INSTITUTE OF PHYSICS PUBLISHING PHYSICS IN MEDICINE AND BIOLOGY

Phys. Med. Biol. **49** (2004) 2547–2562 PII: S0031-9155(04)75164-7

Feasibility of a novel design of high resolution parallax-free Compton enhanced PET scanner dedicated to brain research*

A Braem[1], M Chamizo Llatas[2], E Chesi[1], J G Correia[3], F Garibaldi[4], C Joram[1], S Mathot[1], E Nappi[5], M Ribeiro da Silva[6], F Schoenahl[7], J Séguinot[1], P Weilhammer[1] and H Zaidi[7]

[1] CERN, PH Department, CH-1211 Geneva, Switzerland
[2] Department of Corpuscular and Nuclear Physics, Geneva University, Geneva, Switzerland
[3] Instituto Tecnologico e Nuclear, Sacavém, Portugal
[4] Instituto Superiore di Sanita, Roma, Italy
[5] INFN, Sezione di Bari, Bari, Italy
[6] Centro de Física Nuclear da Universidade de Lisboa, Lisboa, Portugal
[7] Division of Nuclear Medicine, Geneva University Hospital, CH-1211 Geneva, Switzerland

E-mail: habib.zaidi@hcuge.ch

Received 23 January 2004, in final form 30 March 2004
Published 26 May 2004
Online at stacks.iop.org/PMB/49/2547
DOI: 10.1088/0031-9155/49/12/006

Abstract

A novel concept for a positron emission tomography (PET) camera module is proposed, which provides full 3D reconstruction with high resolution over the total detector volume, free of parallax errors. The key components are a matrix of long scintillator crystals and hybrid photon detectors (HPDs) with matched segmentation and integrated readout electronics. The HPDs read out the two ends of the scintillator package. Both excellent spatial (x, y, z) and energy resolution are obtained. The concept allows enhancing the detection efficiency by reconstructing a significant fraction of events which underwent Compton scattering in the crystals. The proof of concept will first be demonstrated with yttrium orthoaluminate perovskite (YAP):Ce crystals, but the final design will rely on other scintillators more adequate for PET applications (e.g. LSO:Ce or $LaBr_3$:Ce). A promising application of the proposed camera module, which is currently under development, is a high resolution 3D brain PET camera with an axial field-of-view of ∼15 cm dedicated to brain research. The design philosophy and performance predictions based on analytical calculations and Monte Carlo simulations are presented. Image correction and reconstruction tools required to operate this transmissionless device in a research environment are also discussed. Better or similar performance parameters were obtained compared to other known designs at lower fabrication cost. The axial

* All the authors are members of the CIMA Collaboration.

geometrical concept also seems to be promising for applications such as positron emission mammography.

1. Introduction

Advances in quantification of brain function (blood flow, metabolism and receptor characteristics) with positron emission tomography (PET), especially for small structures, rely on two aspects: (i) improvements in instrumentation to enhance imaging performance parameters (e.g. spatial resolution and sensitivity), and development of components to correct for physical degrading factors (e.g. transmission scanning-based attenuation correction); and (ii) improvements in algorithmic design to attain better image quality and achieve more accurate and automated quantification of physiological parameters of interest in clinical and research settings (Zaidi and Sossi 2004). The challenge for advanced PET instrumentation is the optimization of the performance in terms of spatial resolution, contrast and sensitivity, at minimized fabrication and operation cost of the PET scanner (Phelps and Cherry 1998). As PET has become of more interest for clinical practice, several different design trends seem to have developed (Phelps 2000). Systems are being designed for 'low cost' clinical applications, very high resolution research applications, and just about everywhere in-between. All of these systems are undergoing revisions in both hardware and software components to meet the requirements of both clinical and research investigators.

New detector technologies that are emerging encompass the use of new scintillating materials as detectors including new cerium-doped, fast and high-effective-Z crystals such as gadolinium orthosilicate (GSO:Ce), lutetium oxyorthosilicate (LSO:Ce), lutetium orthoaluminate perovskite (LuAP:Ce) and lanthanum halide scintillators ($LaBr_3$:Ce) as alternatives to conventional bismuth germanate (BGO) crystals (Moses 2002), the use of layered crystals and other schemes for depth-of-interaction (DOI) determination. Significant progress has been made by different scanner manufacturers and research groups in the design of high resolution 3D PET units with the capacity to acquire more accurate DOI information to reduce the parallax error. However, emerging clinical and research applications of functional brain imaging demand even greater levels of accuracy and precision and therefore impose more constraints on hardware and software aspects, especially with respect to the intrinsic performance of the PET tomograph (Zaidi and Sossi 2004). Continuous efforts to integrate recent research findings for the design of PET scanners have become the goal of both the academic community and nuclear medicine industry.

Most current commercial dedicated PET scanners employ conventional detector blocks (except the continuous positioning detector technology used by Philips Medical Systems) consisting of several stacked rings of inorganic scintillating crystals radially oriented and readout on the backside by standard photomultiplier tubes (PMTs) or multi-anode PMTs. The DOI of the detected photons in the crystal is not measurable in such a configuration and gives rise to intrinsic parallax errors, hence an image degradation depending on the emission point in the transaxial plane and/or the angle of incidence of the lines of responses (LoRs) (figure 1). This effect becomes worse when reducing the scanner's ring diameter or the size of the crystal's cross-sectional area. This inherent limitation could be coped with by keeping the radial length of the crystal small, typically on values around the attenuation length at 511 keV, which however strongly compromises the detection efficiency. The phoswich approach, which leads to a better approximation of the interaction point, has recently been implemented in several designs and particularly in the ECAT high resolution research

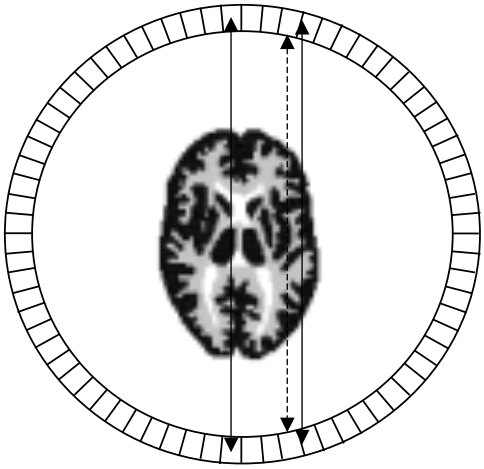

Figure 1. Illustration of the parallax or depth of interaction error associated with annihilations occurring off-centre of the transaxial field-of-view or oblique LoRs for a cylindrical multi-ring PET scanner.

tomograph (HRRT) (Wienhard *et al* 2002), which we consider as the current reference in commercial brain PET technology compared to other prototype designs including G-PET (Karp *et al* 2003) and SHR-12000 (Watanabe *et al* 2002). Such an approach halves the parallax error for a given crystal length, but still only represents a compromise between maximum sensitivity and optimum spatial resolution. The limitations related to intrinsic physical performance of conventional designs encourage the development of innovative approaches capable of providing improved performance at a reduced or comparable cost. In PET systems designed for human brain imaging, improved performance in terms of spatial resolution, sensitivity and signal-to-noise ratio may be achievable using finely segmented arrays of high-Z scintillation crystals coupled to highly pixelized photodetectors in a geometry which allows reconstructing the interaction point of the annihilation photon in true 3D.

In this perspective, we propose a novel 3D brain PET concept[8], which is complementary to existing commercial (Wienhard *et al* 2002) and prototype PET tomographs currently under development (Watanabe *et al* 2002, Karp *et al* 2003). This concept leads to an image reconstruction which is free of any parallax error and provides a uniform spatial and energy resolution over the whole sensitive volume (Braem *et al* 2003c). Furthermore, it allows enhancing the sensitivity by reconstructing a substantial fraction of events which underwent Compton scattering in the detectors. This paper describes the principles of this new concept and the design philosophy as well as the basic components of the PET camera modules under development within the framework of the computer imaging for medical applications (CIMA) collaboration[9] hosted by CERN. Considering the analytical calculations and preliminary Monte Carlo simulations presented herein supported by some recent experimental measurements (Braem *et al* 2004) and detailed comparisons between calculations and Monte Carlo simulations for different configurations (Séguinot *et al* 2004), it seems that this technology is promising for future designs of high resolution PET scanners. It was therefore felt that this preliminary report will be of interest to the medical imaging community prior to actual construction of the prototype.

[8] Patent applied for PCT/EP 02/07967.
[9] http://www.cima-collaboration.org/.

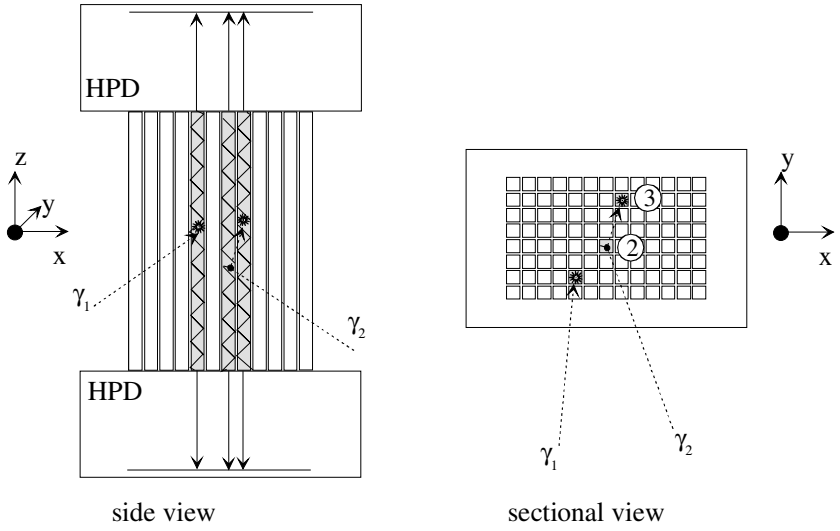

Figure 2. Principle of the HPD-based 3D Compton-enhanced PET camera module.

2. Materials and methods

2.1. The HPD-PET concept

Over the last few years, the European Organization for Nuclear Research (CERN) has expanded the facilities to develop and build hybrid photon detectors (HPDs) including designs with a proximity focused optics and thin sapphire entrance windows. The proposed innovative HPD 3D axial detector concept is based on recent substantial development efforts in high energy physics instrumentation, undertaken at CERN in collaboration with other research institutes, universities and companies. A key component is the large area highly pixelized HPD with its integrated self-triggering readout electronics (Joram 1999, Weilhammer 2000, Braem *et al* 2003a). The particular features of this photodetector technology allow for a cost efficient readout of finely segmented arrays of scintillator crystals.

Our 3D brain PET concept overcomes the parallax problem by means of a novel geometric configuration (Braem *et al* 2003b). The proposed 3D PET camera module consists of an array of long (100–150 mm) crystals of small cross-section (e.g. 3.2×3.2 mm^2). This axially oriented array of crystals (e.g. 13×16) is read out on both sides by HPDs. Figure 2 shows the principle of the 3D HPD-based Compton-enhanced PET design. The size and segmentation of the silicon sensor matches exactly the crystal matrix. This highly segmented geometry provides an accurate and uniform resolution in the transaxial (x–y) plane, completely independent of the radial detector thickness. The latter can therefore be increased by two to three attenuation lengths, which essentially doubles the sensitivity compared to the HRRT equipped with the conventional phoswich block detector approach. The transaxial segmentation allows tracking multiple interactions of annihilation photons in the scintillator matrix, which provides the possibility of reconstructing a large fraction of Compton scattered events. This results in a further sensitivity increase by a factor of 1.5–3 depending on crystal material and size. The axial coordinate (z) is derived with good precision from the asymmetry of the light intensity detected at the two ends of the scintillating crystals. Hence, the coincident event is reconstructed in fully 3D mode without any parallax effects irrespective of the annihilation

Table 1. Characteristics of scintillator crystals under development and currently used in commercial and prototype PET tomographs design.

Scintillator	BGO	LSO	GSO	LuAP	$LaBr_3$	YAP
Formula	$Bi_4Ge_3O_{12}$	Lu_2SiO_5:Ce	Gd_2SiO_5:Ce	$LuAlO_3$:Ce	$LaBr_3$:Ce	$YAlO_3$:Ce
Density (g cc^{-1})	7.13	7.4	6.71	8.34	5.3	5.37
Light yield (photons/keV)	9	25	8	10	61	21
Effective Z	75	66	60	65	46.9	34
Principal decay time (ns)	300	42	30–60	18	35	25
Peak wavelength (nm)	480	420	440	365	358	370
Index of refraction	2.15	1.82	1.95	1.95	1.88	1.94
Photofraction (%)[a]	41.5	32.5	25	30.6	15	4.5
Attenuation length (cm)[a]	1.04	1.15	1.42	1.05	2.13	2.19
Energy resolution (%)[a]	7.9	8	6.9	10	2.9	3.8
Hygroscopic	No	No	No	No	Yes	No

[a] At 511 keV.

point. This is expected to lead to a spatial and energy resolution, which is superior to any known comparable system and completely uniform over the whole detection volume. A remarkable improvement in image quality and quantitative accuracy could consequently be attained. The achievable spatial and energy resolution as well as the sensitivity depend on the choice of the scintillation crystal and will be discussed in the following sections. In addition to YAP, some companies already confirmed the possibility of providing long crystals with the dimensions quoted in this paper. These can be either LYSO manufactured by Photonic Materials Ltd (Bellshill, UK) or LSO manufactured by CTI Molecular Imaging (TN). The collaboration is also discussing with Saint Gobain (France) the possibility of manufacturing long lanthanum bromide scintillators ($LaBr_3$).

2.2. Design considerations

The steps required to build the PET camera modules with the specifications claimed above comprise several distinct major components or work blocks, for which a well-defined sharing of responsibilities amongst the participating institutes has been defined. The hardware components, characterization and validation of the prototype under development are described below.

2.2.1. The scintillator matrix. The choice of the scintillator is a fundamental element of a PET design. The prototype design will profit from recent progress in the development and growing of crystals with optimized characteristics and the associated machining (cutting and polishing) techniques. On the medium term cerium doped lutetium orthosilicate (LSO:Ce), produced by CTI molecular imaging (Knoxville, TN) and cerium doped lanthanum bromide ($LaBr_3$:Ce), under development by Saint Gobain (France), are the most promising candidates. They combine high density and high atomic number necessary for an efficient photoelectric conversion of the annihilation photons, with a short decay time of the scintillation light, which is a key requirement for high counting rates. Table 1 summarizes these properties for selected scintillators currently in use and under development for PET applications. The final choice will be made after an in-depth investigation of the physical characteristics including light yield, energy resolution, linearity of response with energy, light absorption coefficient at wavelength of emission, mechanical properties and surface quality of long crystal bars, availability and cost.

An advantage of LSO compared to $LaBr_3$ is its high photoelectric cross section, but it is substantially worse in terms of energy resolution and response linearity. Also the decay time of LSO is longer than the one of $LaBr_3$. However, this crystal is still in a development phase at Saint Gobain and not yet commercially available. It is worth emphasizing that a recent study reported that the combination of excellent energy resolution and timing resolution of $LaBr_3$ can potentially lead to a significant improvement in PET performance (Surti *et al* 2003). To avoid unnecessary delays, the collaboration decided to initially demonstrate the innovative features of the HPD-PET concept and explore its potential with yttrium orthoaluminate perovskite (YAP:Ce) crystals, although its physical characteristics are not optimal for PET applications. The motivation behind this choice is that the material is inexpensive, commercially available and can be machined and polished to long bars.

For the 3D axial detector geometry shown in figure 3, 208 (13×16) long crystals of 3.2×3.2 mm^2 cross section are arranged to a matrix with gaps of 0.8 mm between crystals. Scintillation light, produced after an interaction of an annihilation photon, propagates by total internal reflection to the ends, where it is detected by the HPD photodetectors. The transaxial resolution depends only on the crystal segmentation and not on its chemical composition while the axial resolution is closely related to the scintillator properties. The value of the scintillator's optical bulk absorption length needs to be of the same order as the crystal length in order to obtain a high light yield and at the same time to produce a significant light asymmetry required for the determination of the axial coordinate z.

2.2.2. Hybrid photon detectors. Hybrid photon detectors represent one of the most promising options for high granularity photon detection (Joram 1999). An HPD consists of a phototube with two key components: a semi-transparent photocathode with high sensitivity for photons in the visible and near UV range, which is deposited by vacuum evaporation on the entrance window and a silicon (Si) sensor playing the role of the anode (Weilhammer 2000). Figure 4 illustrates the principle of operation and shows a photograph of an HPD. The photocathode converts incident photons to electrons. These photoelectrons are accelerated by an electrostatic field (10–20 kV between cathode and anode), which is shaped by a set of ring electrodes, onto the segmented Si sensor and create a signal proportional to their kinetic energy. Basically, the HPD combines the sensitivity to single photons of a conventional PMT with the spatial and energy resolution of a solid state sensor. The intrinsic limitations of a classical PMT owing to the statistical fluctuations in the number of electrons at the first dynodes are completely overcome.

The photodetectors, which are coupled to both ends of the crystal array, are proximity focused HPDs with a thin (1.8 mm) flat sapphire entrance window. Keeping this window as thin as possible minimizes the widening of the light cone when it propagates from the scintillation crystal to the photocathode of the HPD deposited on the inner surface of the window. The quantum efficiency of the photocathode is about 25% at the wavelength of maximum emission of $LaBr_3$ and $\sim$18% for LSO. The proximity focusing electron optics of the HPD produces a 1:1 image of the scintillator array onto the silicon sensor, which is segmented into 208 (13×16) diode pads of 4×4 mm^2 size, precisely matching the pattern of the crystal array. The sensor is mounted on a ceramic carrier which receives the two front-end chips (type VATA, 128 channels/chip, see section 2.2.3). Wire bonds link the chips to the sensor. The HPDs are operated at a moderate cathode potential of about 12 kV, sufficient for a signal of about 3000 electron–hole pairs in the silicon sensor for every detected photoelectron. The point spread function, which describes the Gaussian width of the charge distribution on the silicon for a point-like light source, is of the order of 0.3 mm.

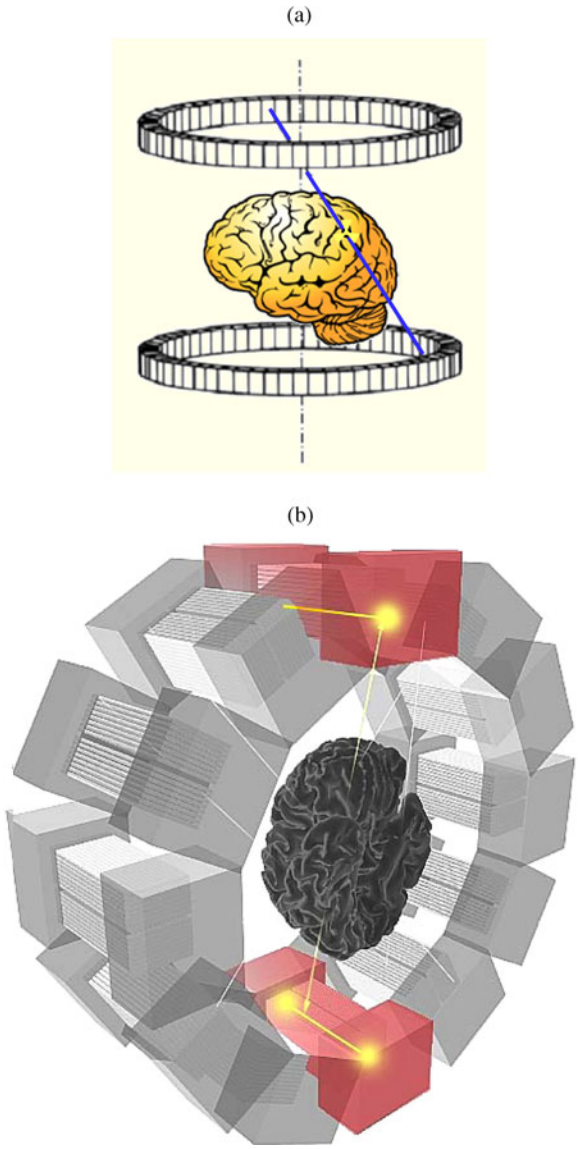

Figure 3. Illustration of principles of data acquisition for a brain PET camera using the conventional cylindrical multi-ring geometry based on detector blocks and readout by PMTs (a) and the novel design based on 12 camera modules consisting of long scintillation crystals readout on both sides by HPDs (b).

While in the initial phase of the prototype construction, a round HPD with ceramic body will be used to assemble a PET camera module for the proof of principle, the early demonstrator requires a rectangular HPD with optimized geometry to increase the inner free diameter of the scanner and improve the azimuthal coverage. During the last few years, the CERN group has built numerous HPDs with a diameter of 127 mm and 16 readout chips (2048 channels) encapsulated inside the vacuum envelope (Braem *et al* 2003a). The complex technical facilities for the preparation of components and the photocathode processing and

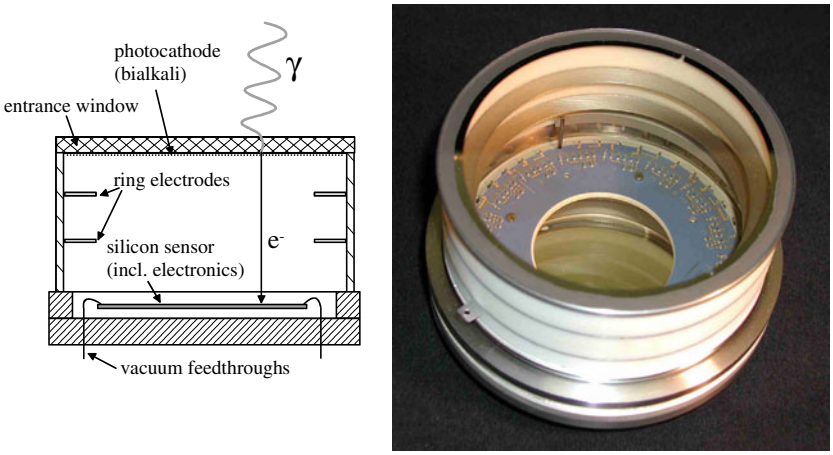

Figure 4. Schematic drawing (a) and photograph (b) of proximity focused hybrid photon detector. The readout electronics (VATA-GP chip set) is encapsulated in the vacuum envelope.

encapsulation of round HPDs are available. A moderate upgrade of the facilities will allow fabricating also rectangular devices.

2.2.3. Front-end electronics. The front-end electronics, which amplifies, shapes, samples and temporarily stores the signal produced in the silicon sensor of the HPD is another key component of the concept. The fast VLSI chip VATA-GP5 is being developed by Ideas ASA[10] in collaboration with CERN on the basis of the VATA-GP3, which recently has been fully characterized (Chesi *et al* 2003). The GP3 version has 128 channels and provides self-triggering operation mode, as required for PET. Each channel comprises (figure 5):

- a 'slow' analogue chain with a charge sensitive amplifier, and a shaper of $\tau_s = 3$ μs time constant for low-noise pulse height determination. The sampled maximum pulse height is stored in a register for later readout;
- a 'fast' chain with additional amplification, fast shaping ($\tau_f = 150$ ns) and discrimination. It is the logical 'OR' of all 128 discriminators, which is interpreted as trigger signal for the readout of the pulse height information.

In contrast to a conventional serial readout mode, where after a trigger all 128 channels would be readout, in sparse mode only those channels with a discriminated hit obtain a readout tag. This feature strongly shortens the overall readout time, particularly if typically only one or very few channels are hit. The current version already comprises numerous features which are indispensable for a PET system like blocking and reset mechanisms, masking, fine adjustment of thresholds and calibration. For a full demonstration of its performance in PET operation, the chip design needs to undergo further development iterations:

- the dynamic range of the input stage is adapted from currently 18 fC to about 400 fC to handle the typical charge level in the silicon detector during PET operation;
- to achieve shaping time constants of 25 and 150 ns, respectively, required for PET coincidence timing in a 5 ns interval and high rate operation, the chip needs to be

[10] Integrated Detector & Electronics, Hovik, Norway.

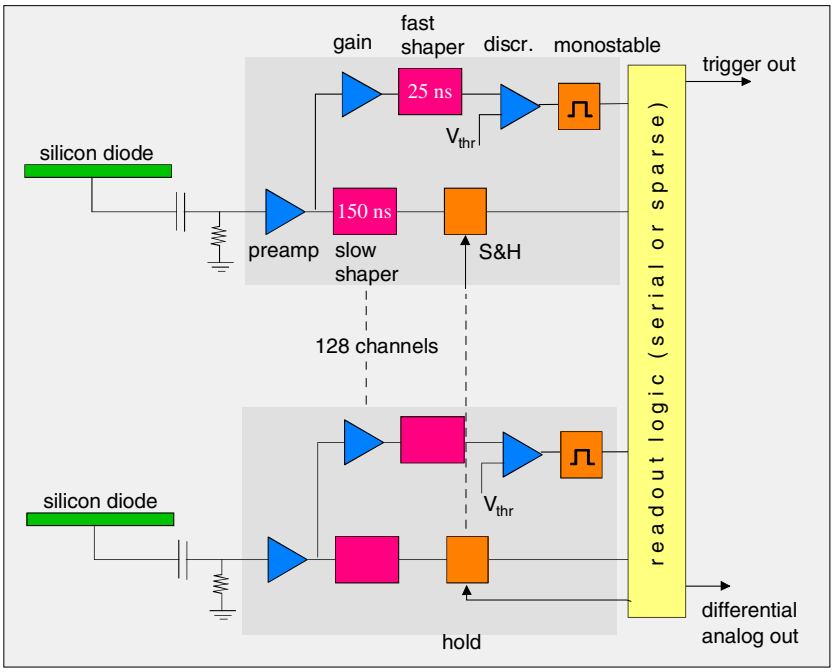

Figure 5. Schematic layout of the VATA-GP3 front-end chip.

implemented in deep sub-micron technology. In addition time walk compensation (or constant fraction discrimination), minimized propagation times of control signals and 20 MHz readout clock speed need to be implemented.

2.2.4. HPD 3D axial camera module. A HPD 3D axial camera module consists of a matrix assembly of 208 (13 × 16) long scintillation crystals, optically coupled to a pair of HPD photodetectors. A first camera module will be fabricated using round HPDs (PCR5) and a matrix of 64 YAP:Ce crystals (figure 6). At a later stage, the full performance of the HPD-PET concept will be demonstrated in an arrangement of four final camera modules employing optimized rectangular HPDs, fast electronics, final scintillation crystals and the PET data acquisition system discussed in the following section.

2.2.5. Data acquisition system. The data acquisition system (DAQ) of the PET camera needs to cope with high single and coincidence count rates as well as high data taking rates. Our approach, tailored to the specific characteristics of the HPD front-end electronics, consists of parallel fast coincidence processors coupled to high density storage media and one asynchronous readout chain for each camera module.

A 'good' PET event is defined as the time-coincident detection of two annihilation quanta of 511 keV energy emitted in a back-to-back configuration. Coincidences are formed on the level of camera modules. The counting rate of each module under the test conditions of the NEMA-NU2 protocol with a cylindrical phantom (20 cm diameter and 20 cm length) of 13 kBq ml^{-1} activity (total activity = 81.4 MBq) is of the order of 1.5 MHz. To limit the rate of accidental coincidences between modules, the coincidence time window was set at 5 ns (comparable to 6 ns set on the HRRT). The final choice will depend on results and

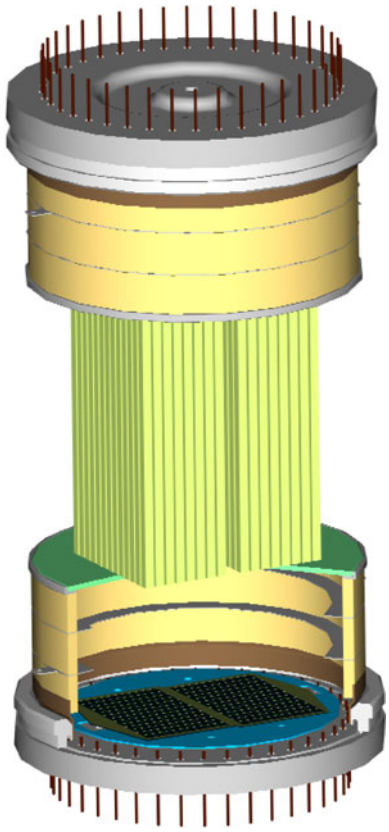

Figure 6. Illustration of a 3D PET camera module. In this prototype configuration two round HPD photodetectors are coupled to the matrix of scintillators.

performances obtained on the experimental prototype under development. Reading out the information stored in the four front-end chips of a module leads to a dead-time fraction of less than 10%. The concept of parallel coincidence processors permits to initiate the readout sequence only for those two modules which form a coincidence, while all other modules stay active, thus minimizing the system dead-time. We expect the parallel readout chains to record the (trues+scatter) data of each module at a rate of about 200 kHz. The raw data will be stored on fast hard disks of at least 200 GB storage capacity.

2.3. HPD-PET performance predictions and Monte Carlo modelling

To evaluate the expected performance of the above-described detector camera module, analytical calculations have been performed, some of which have been supported by Monte Carlo (MC) simulations. There exist many MC simulation packages running under standard operating system environments, which are easily extendible to new scanners' geometrical configurations. In this study, calculations and simulations using GEANT4 (Agostinelli *et al* 2003) and EGS4 (Nelson *et al* 1985) MC codes have been performed in order to characterize the performance of the system (Chamizo Llatas *et al*, personal communication). Photon transport in the long scintillator bars and detection resolution has been simulated with a custom MC code. The code is able to track individual scintillation photons from the emission

point through the crystal to the photodetectors, taking into account refraction and reflection at all optical boundaries, as well as absorption. It also includes the photon detection process in the HPD. In the following, we sketch a performance estimate based on 15 cm long LSO:Ce crystals. The detailed calculations and simulation parameters are described in an accompanying paper (Séguinot *et al* 2004) and will not be repeated here.

3. Results

3.1. Photon transport and detection

The total number of photons N_{det} detected at both (left and right) ends of the crystals is given by

$$N_{\text{det}} = N_L + N_R = \frac{N_{\text{ph}}}{2}\varepsilon_C\varepsilon_Q\left(\mathrm{e}^{-\frac{z}{\lambda^*}} + \mathrm{e}^{-\frac{(L-z)}{\lambda^*}}\right) \tag{1}$$

where N_{ph} is the number of produced scintillation photons following the absorption of a 511 keV quanta (0.511 MeV $\times$ 23 000 MeV^{-1} = 11 750). The light transport efficiency ($\varepsilon_C = 0.62$) has been determined by means of microscopic photon tracking MC calculations, which take into account reflection and refraction at all optical interfaces. The effective light absorption length (λ^*) differs from the bulk absorption length, in view of the fact that it takes into account the real pathlength of the optical photons when they bounce from the crystal walls. This was estimated by MC simulations to be $\lambda^* \approx 0.8\ \lambda_a$. The bulk optical absorption length (λ_a) of LSO is not known yet and has been assumed to be 100 mm. The quantum efficiency of the photosensor ε_Q is 0.18 at the wavelength 420 nm (bialkali PC). The distance z of the interaction point is measured from the end of the crystal with total length L. Considering only 'photoelectric events', the absorption of 511 keV annihilation photons in the LSO crystals leads to between 480 ($z = L/2$) and 680 (at the bar ends, i.e. $z = 0$ or $z = L$) detected scintillation photons.

3.2. Energy resolution

The energy resolution $R = (\Delta E/E)_{\text{FWHM}}$ is estimated from combined contributions of the scintillator, statistical and noise terms:

$$R = \sqrt{R_{\text{sci}}^2 + R_{\text{stat}}^2 + R_{\text{noise}}^2}. \tag{2}$$

The intrinsic resolution R_{sci} of LSO due to material inhomogeneity, coupling between scintillator and photodetector and nonlinear energy response has been measured to be ~6.5% at 511 keV (Moses 2002). R_{stat} represents the statistical fluctuation involved in the light generation and detection process, including the photodetectors $R_{\text{stat}} = 2.35/\sqrt{N_{\text{det}}} \sim 9.7\%$ (average). The single stage dissipative gain mechanism of the HPD operated at 12 kV leads to a negligible contribution to R_{stat}. Also the electronics noise of the detection chain contribution (R_{noise}) is very small compared to the other two terms. Thus, the resulting energy resolution R at 511 keV is about 11.7%.

3.3. Determination of the interaction point

In the transaxial x–y plane, the coordinates of the photon interaction point in the scintillator are derived from the address of the hit crystal. The resolution is determined by the dimensions of the crystals (s):

$$\sigma_x = \sigma_y = \frac{s}{\sqrt{12}} \tag{3}$$

with $s = 3.2$ mm being the size of the crystals in the transverse direction. The spatial resolution of the HPD is matched to this value and does not contribute. The x and y coordinates of the photons' interaction points can be reconstructed with a precision of better than 2.2 mm (FWHM). The axial z coordinate is derived from the measurement of the asymmetry of the amount of light detected at the two sides of the crystal and is thus dependent on the attenuation length of the crystal,

$$z = \frac{1}{2}\left[\lambda^* \ln\left(\frac{N_L}{N_R}\right) + L\right]. \tag{4}$$

Error propagation of the above equation leads to a resolution in the axial coordinate ranging from $\sigma_z/L = 2.5\%$ in the middle of the crystal ($z = L/2$) to $\sigma_z/L = 2.7\%$ at the ends. For the proposed geometry ($L = 15$ cm), the z coordinate of 511 keV photons can thus be reconstructed with a precision of ∼9 mm (FWHM). A MC study modelling precisely the geometry of the design described above, where both annihilation photons are tracked independently taking into account effects such as positron range and non-collinearity of the two annihilation photons, leads to a reconstruction resolution of the emission point of $R_x = R_y \approx 2$ mm (FWHM) and $R_z \sim 5.5$ mm (FWHM). A detailed description of this study is described elsewhere (Séguinot *et al* 2004).

3.4. Sensitivity and Compton enhancement

The 3D axial PET concept is intrinsically free of parallax errors and therefore allows increasing the detector thickness without compromising the spatial resolution. The above described geometry (13 rows of LSO crystals) corresponds to more than $3\lambda_{\text{att}}$. The effective solid angle of the detector has been determined by MC calculations, assuming the same cylindrical phantom as described for the HRRT (Wienhard *et al* 2002). Taking into account only events converted by photoeffect, an absolute detection efficiency of 2.7 cps kBq^{-1} ('trues' only) is found (Séguinot *et al* 2004).

The full 3D reconstruction and the large envisaged detection volume allow taking into account a substantial fraction of photons, which first underwent Compton scattering in one of the crystals and are then detected by photoelectric effect in another, without compromising the spatial resolution. The total energy is reconstructed by summing up the energies of all hit bars. To unambiguously distinguish between the coordinate of the primary Compton interaction (to be used in the 3D reconstruction algorithm) and the coordinate of the final absorption of the photon (by photoelectric effect), only events in which the photon was scattered into the forward hemisphere are selected. The criteria for the event selection are derived from the Klein–Nishina (KN) formula, which describes the energy and angle-dependent Compton cross-section and the Compton kinematics. The latter defines the energies of the recoil electron E_e and the scattered photon E_s as a function of the initial photon energy E and scattering angle θ,

$$E_s = \frac{E}{1 + (E/m_0c^2)(1 - \cos\theta)} \qquad \text{and} \qquad E_e = E - E_s. \tag{5}$$

The analysis of the Compton kinematics shows that part of the events, which undergo Compton scattering before photoelectric absorption, can be reconstructed if the photons are scattered at forward angle ($\sim 30^\circ < \theta < 60^\circ$). These events have a clear signature with an energy deposit in the first interaction (seen from the centre of the PET scanner) in the range [50–170] keV and a second interaction with the corresponding remaining energy [340–460] keV. The KN formula shows that ∼25% of all events fall in this category. The Compton scattered events at greater angles are 'ambiguous', as the energy deposits in the

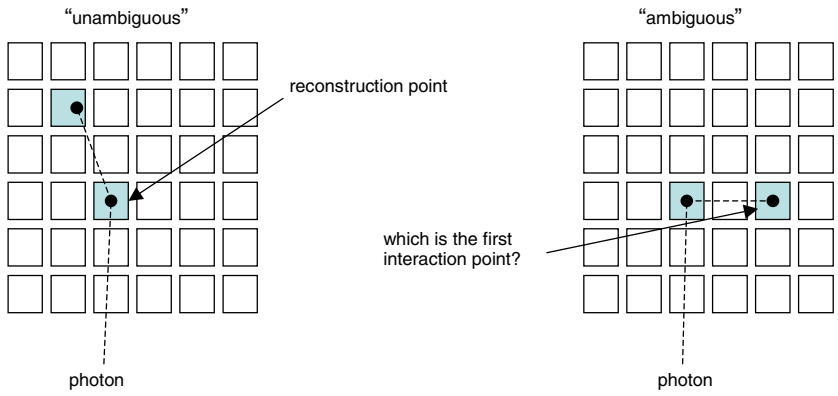

Figure 7. Illustration of detector Compton-scattered events. To unambiguously distinguish between the coordinate of the primary Compton interaction and the coordinate of the final absorption of the photon, only events in which the photon was scattered into the forward hemisphere are selected. Events undergoing Compton scattering before photoelectric absorption can be reconstructed if photons are Compton scattered at forward angles ($\sim 30^\circ < \theta < 60^\circ$). That is, when the energy deposit in the first interaction is in the range [50–170] keV (25% of all events fall in this category). The Compton scattered events at greater angles are 'ambiguous' and cannot be reconstructed.

two interactions are very similar. These events cannot be reconstructed (figure 7) because no distinction can be made between first and second interactions. The 'Compton gain' from including the above-described forward events is estimated to be $\sim$1.8 (Séguinot *et al* 2004), which leads to an absolute sensitivity of $\sim$5 cps kBq^{-1}.

4. Discussion

The limitations of current PET instrumentation dedicated to brain imaging motivate the development of new technologies capable of responding to current needs of clinical and research neuroscience investigators (Zaidi and Sossi 2004). We have described a novel concept for the design of a PET camera module dedicated for brain research, which provides full 3D reconstruction with high resolution over the total detector volume, free of parallax errors. Subdividing the scintillator into fine crystal bars, as is required for the true 3D readout and the Compton reconstruction approach, leads to a very large number of readout channels. This needs to be coped with by pixelized photodetectors with sufficient gain, excellent linearity and no cross talk. Sophisticated VLSI front-end electronics and parallel DAQ architectures are indispensable to handle the enormous data stream generated by such a device. For optimal PET sensitivity, the identification and reconstruction of photons which underwent Compton scattering in the detector is the most promising strategy. This approach becomes feasible if the photon interaction points in the crystal matrix can be measured in true 3D. It is then possible to track the photon through the scintillator and unambiguously reconstruct a significant fraction of Compton scattered events.

The HRRT has a field-of-view (FOV) of 25.2 cm axially and 31.2 cm transaxially. It achieves a spatial resolution (FWHM) of 2.4 mm at the centre of the FOV and 2.8 mm at 10 cm off-centre transaxially and 2.6 to 5.2 mm axially depending on axial compression mode (span) and reconstruction procedure. The energy resolution varies between 14 and 18% (Schmand *et al* 1998). An absolute sensitivity of 4.4 cps kBq^{-1} ('trues' only) and a maximum

noise equivalent count (NEC) rate of 230 kcps reached at 37 kBq ml^{-1} have been measured with a cylinder of 20 cm diameter and 20 cm length filled with ^{18}F dissolved in water.

The high light output of the LSO:Ce crystal bars, combined with the excellent pulse height resolution of the HPD, results in a system energy resolution of ∼11.7% (FWHM), which is significantly better than resolutions quoted for existing systems. The interaction point in the crystals can be determined with a spatial resolution in the transaxial and axial coordinates of 2.2 and 9 mm (FWHM), respectively. Both the axial spatial and energy resolutions would significantly improve if $LaBr_3$ crystals become available. Detailed calculations for a brain PET scanner with 34 cm free inner diameter and 15 cm axial FOV (figure 3), based on the proposed axial approach and equipped with LSO:Ce or $LaBr_3$:Ce crystals, let expect an absolute sensitivity of ∼5 cps kBq^{-1}. This value is higher than that quoted for the HRRT scanner, one of the most advanced systems, which has however an axial FOV of 25 cm (compared to 15 cm in our design).

The collaboration is developing the required software packages to correct the data for physical degrading effects (attenuation, scatter, partial volume effects, etc) and reconstruct images from measured data as well as the graphical user interface and image display and analysis utilities required to validate and exploit the system in a clinical and research environment. The events are collected in list-mode format to enable direct list-mode iterative reconstruction, which is preferred to projection-based reconstruction when high resolution imaging is sought (Bouwens *et al* 2001). An undesirable property of the iterative maximum likelihood expectation-maximization (ML-EM) algorithm is that large numbers of iterations increase the noise content of the reconstructed images. These noise characteristics can be controlled in iterative algorithms that incorporate a prior distribution to describe the statistical properties of the unknown image and thus produce *a posteriori* probability distributions from the image conditioned upon the data. Bayesian reconstruction methods form a powerful extension of the ML-EM algorithm (Green 1990). Maximization of the *a posteriori* (MAP) probability over the set of possible images results in the MAP estimate (Qi and Leahy 2000). The reconstruction package is based on an updated version of the STIR open source reconstruction library[11] to reconstruct images from data acquired in list-mode format.

To obtain quantitative PET data, it is necessary to estimate and correct for major physical factors that degrade the acquired data. The non-homogeneous distribution of attenuation coefficients due to presence of air cavities and sinuses complicates the interpretation of 3D brain PET images and precludes the application of simple methods of scatter and attenuation correction developed for homogeneous media. Moreover, the problem of scatter correction is of paramount importance in high resolution PET imaging in which the scatter degradation features become more complex. Therefore, we are focusing on correction schemes for resolution recovery, and attenuation and scatter corrections integrated in the reconstruction process. A transmission scanning component is not planned on this device to reduce the development cost and avoid unnecessary complexity of the design. Models for accurate quantification using co-registered MRI and PET data developed at Geneva University Hospital will also be further developed to include MRI-guided partial volume effect correction and used on this transmissionless device (Zaidi *et al* 2003, 2004).

Further research will focus on full simulation of the prototype design aspects. The Monte Carlo software package with which the authors have some experience consists of a modified version of a PET simulator based on GEANT platform (Agostinelli *et al* 2003), developed previously for the cylindrical multi-ring geometry (Zaidi *et al* 1999) but extendible to any design geometry. This package is being further developed and exploited to optimize the design of the HPD-PET scanner.

[11] http://stir.irsl.org/.

5. Conclusion

A novel concept for a PET camera module is described and its expected performance parameters assessed, which provides full 3D reconstruction with high resolution over the total detector volume, free of parallax errors. The main novelty of the proposed design is the arrangement of detectors in an axial geometry and the elimination of parallax error without using a phoswich detector, which we believe is unnecessary. In addition, our design uses silicon sensors and HPDs, which have been used for the first time in the PET imaging area. The CIMA collaboration at CERN is actively engaged in the construction of this new device to support ongoing research activities aiming at understanding functionalities of the human brain. The concept also seems to be promising for positron emission mammography (PEM) where both high spatial resolution and sensitivity are required to meet the needs of early detection of breast tumours, hence avoiding biopsy intervention.

Acknowledgments

We would like to thank Professors J-M LeGoff and R Amendolia (CERN ETT-TT) for the continuous support of this project. The construction of the prototype HPDs would not have been possible without the competent work of numerous technical collaborators, particularly C David and I Mcgill (CERN PH-TA1). This work was supported by the Swiss National Science Foundation under grant SNSF 3152A0-102143.

References

Agostinelli S *et al* 2003 GEANT4—a simulation toolkit *Nucl. Instrum. Methods* A **506** 250–303

Bouwens L *et al* 2001 Resolution recovery for list-mode reconstruction in SPECT *Phys. Med. Biol.* **46** 2239–53

Braem A *et al* 2004 Novel design of a parallax free Compton enhanced PET scanner *Nucl. Instrum. Methods* A at press

Braem A *et al* 2003a The Pad HPD: a highly segmented hybrid photodiode *Nucl. Instrum. Methods* A **497** 202–5

Braem A *et al* 2003b Novel design of high-resolution parallax-free Compton enhanced PET scanner dedicated to brain research *Conf. Proc. 1st Int. Meeting on Applied Physics (Badajoz, Spain, 15–18 Oct. 2003)* pp 86–67

Chesi E *et al* 2003 The VATAGP3 test set-up and first results from measurements with the VATAGP3 chip *Nucl. Instrum. Methods* A (submitted)

Green P J 1990 Bayesian reconstructions from emission tomography data using a modified EM algorithm *IEEE Trans. Med. Imaging* **9** 84–93

Joram C 1999 Large area hybrid photodiodes *Nucl. Phys.* B **78** 407–15

Karp J S *et al* 2003 Performance of a brain PET camera based on anger-logic gadolinium oxyorthosilicate detectors *J. Nucl. Med.* **44** 1340–9

Moses W W 2002 Current trends in scintillator detectors and materials *Nucl. Instrum. Methods* A **487** 123–8

Nelson W R, Hirayama H and Rogers D W O 1985 The EGS4 code system *SLAC-256 (Stanford Linear Accelerator Center, Stanford, CA)*

Phelps M E 2000 PET: the merging of biology and imaging into molecular imaging *J. Nucl. Med.* **41** 661–81

Phelps M E and Cherry S R 1998 The changing design of positron imaging systems *Clin. Pos. Imaging* **1** 31–45

Qi J and Leahy R M 2000 Resolution and noise properties of MAP reconstruction for fully 3-D PET *IEEE Trans. Med. Imaging* **19** 493–506

Schmand M *et al* 1998 Performance results of a new DOI detector block for a high resolution PET-LSO research tomograph HRRT *IEEE Trans. Nucl. Sci.* **45** 3000–6

Séguinot J *et al* 2004 Design and performance of a 3D axial PET scanner (submitted)

Surti S *et al* 2003 Investigation of lanthanum scintillators for 3-D PET *IEEE Trans. Nucl. Sci.* **50** 348–54

Watanabe M *et al* 2002 A new high-resolution PET scanner dedicated to brain research *IEEE Trans. Nucl. Sci.* **49** 634–9

Weilhammer P 2000 Silicon-based HPD development: sensors and front ends *Nucl. Instrum. Methods* A **446** 289–98

Wienhard K *et al* 2002 The ECAT HRRT: performance and first clinical application of the new high resolution research tomograph *IEEE Trans. Nucl. Sci.* **49** 104–10

Zaidi H, Herrmann Scheurer A and Morel C 1999 An object-oriented Monte Carlo simulator for 3D positron tomographs *Comput. Meth. Prog. Biomed.* **58** 133–45

Zaidi H, Montandon M-L and Slosman D O 2003 Magnetic resonance imaging-guided attenuation and scatter corrections in three-dimensional brain positron emission tomography *Med. Phys.* **30** 937–48

Zaidi H, Montandon M-L and Slosman D O 2004 Attenuation compensation in cerebral 3D PET: effect of the attenuation map on absolute and relative quantitation *Eur. J. Nucl. Med. Mol. Imaging* **31** 52–63

Zaidi H and Sossi V 2004 Correction for image degrading factors is essential for accurate quantification of brain function using PET *Med. Phys.* **31** 423–6